JATIS Journal of Astronomical Telescopes, Instruments, and Systems

RESEARCH PAPER

Radiation tolerance of a single-photon counting complementary metal-oxide semiconductor image sensor

Justin P. Gallagher,[a,*] Lazar Buntic,[a] Wei Deng,[b] Eric R. Fossum,[b] and Donald F. Figer[a]

[a]Rochester Institute of Technology, Center for Detectors, Rochester, New York, United States
[b]Dartmouth College, Thayer School of Engineering, Hanover, New Hampshire, United States

ABSTRACT. We present the results of a radiation test program for a 1-megapixel single-photon-counting and photon-number-resolving CMOS image sensor. The results include pre- and post-radiation values for dark current, voltage shift at the pixels' output, read noise, quantum efficiency (QE), conversion gain, and photon counting ability. The Center for Detectors at the Rochester Institute of Technology exposed the sensor to a 50-krad(Si) dose of 60-MeV protons, equivalent to the dose absorbed over 10 11-year space missions at L2 with 1-cm aluminum shielding. The median dark current of the sensor increased from 0.00085 to 0.0085 $e^-/s/pix$ at 258 K and from 0.0075 to 0.075 $e^-/s/pix$ at 282 K. This is an increase of 2.0 $fA/cm^2/krad(Si)$ and 17.8 $fA/cm^2/krad(Si)$, respectively. Performance in other metrics remained constant: 0.34 e^- median read noise, 85% peak QE at 490 nm, and photon number resolution. We report mostly total ionizing dose and displacement damage dose effects and compare the radiation tolerance of the device to the performance of state-of-the-art charge coupled devices and CMOS devices. The detector exhibits a comparable radiation tolerance to the expected tolerance of modern CMOS devices.

 [DOI: 10.1117/1.JATIS.10.3.036003]

Keywords: CMOS; radiation; proton; single photon counting; photon-number-resolving

Paper 23096G received Aug. 16, 2023; revised Aug. 7, 2024; accepted Aug. 28, 2024; published Sep. 24, 2024.

1 Introduction

Photon-counting detectors enable the most sensitive astrophysics observations. Future strategic astrophysics space missions will observe low photon flux sources in ultralow backgrounds at ultraviolet, visual, and near-infrared wavelengths.[1,2] High-energy particle radiation poses a threat to the long-term performance of instruments used in these missions, potentially degrading their detectors and readout electronics.

CMOS image sensors (CISs) with deep sub-electron read noise (DSERN) resolve individual photons, meeting instrument performance requirements of future National Aeronautics and Space Administration (NASA) flagship missions as recommended by the Pathways to Discovery in Astronomy and Astrophysics for the 2020s (Astro2020)[3] decadal survey. These sensors use a low-capacitance floating diffusion (FD) sense node, resulting in a conversion gain of hundreds of microvolts per electron.[4] Although relevant for future missions, manufacturers often design these types of detectors for commercial use in the low-radiation environment on Earth, and their performance is unknown in high-radiation environments.

*Address all correspondence to Justin P. Gallagher, jpgcfd@rit.edu

2329-4124/2024/$28.00

To characterize the performance of a DSERN CIS before and after exposure to high-energy protons, the team developed a radiation test program that exposed the sensor to 50 krad(Si), equivalent to the L2 on-orbit dose a detector receives over 10 11-year solar cycles. The rest of Sec. 1 describes the sensors. Section 2 describes the hardware used to perform the radiation testing. Section 3 describes the radiation test program; the simulations that determine 50 krad(Si) is equivalent to ~110 years on-orbit at L2 and introduces radiation damage in silicon photodetectors. Section 4 presents the pre- and post-radiation performance results of the image sensor in dark current, read noise, conversion gain, and quantum efficiency (QE). Section 5 summarizes the radiation tolerance of the sensor and compares it to other silicon detectors. Section 6 concludes the paper.

1.1 DSERN CMOS Quanta Image Sensor

A team led by Dr. Eric Fossum developed DSERN CMOS detector platforms over the past decade.[5–8] These detectors, named Quanta Image Sensors (QIS), use Taiwan Semiconductor Manufacturing Company (TSMC)'s 45/65-nm 3D-stacked backside illuminated (BSI) CIS process. Gigajot Technology Inc. commercialized the technology and improved its performance and size in formats up to 163 megapixel.[9–13]

The DSERN CMOS device reported in this work has 20 1-megapixel QISs, each with minor variations to the pixel reset and pixel source follower size and type (Fig. 1). The results in Sec. 4 are from sensor #2, one of the 20 image sensor arrays on chip #1, henceforth referred to as QISSAT1-2. This device represents the first generation megapixel QIS array, whereas later generations include improved devices (e.g., read noise) that exist in commercial forms that are not suitable for cryogenic testing. The characterization work was funded by NASA through a Strategic Astrophysics Technology (SAT) program (PI Figer, 80NSSC20K0310). Table 1 includes information about the QISSAT1-2 image sensor.

The detector resolves the photon number using a distal low-capacitance high-gain FD sense node to increase the conversion gain for a single electron to overcome the voltage noise.[16] The sense node capacitance has contributions from several pixel components including (1) the overlap capacitance from the transfer gate (TG), (2) the overlap capacitance from the reset gate (RG), (3) the source follower gate capacitance, and (4) the intermetal coupling capacitance from wiring (Fig. 2). As an example, consider the low-noise pixels described in Ref. 15 that reduced the effective FD capacitance to 0.464 fF, corresponding to a conversion gain of 345 $\mu V/e^-$.

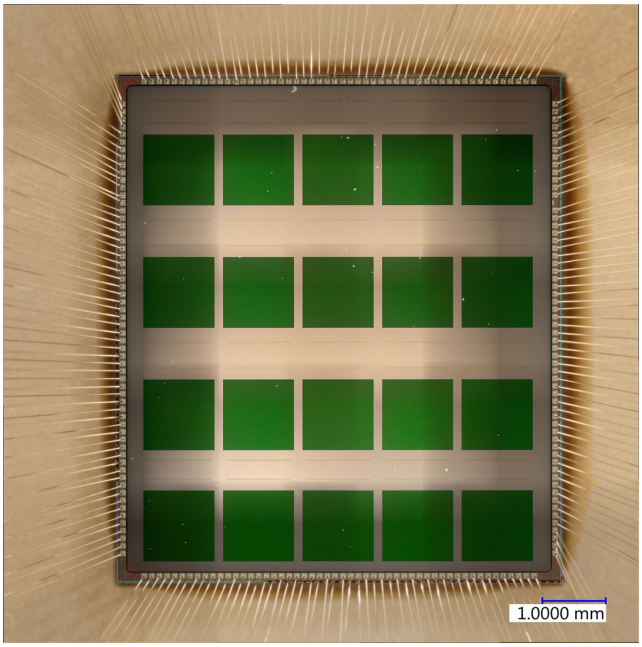

Fig. 1 A silicon die is wirebonded in a chip carrier. The die contains 20 1-Megapixel CMOS image sensors in a grid.

Table 1 QISSAT1-2 detector information.

Pixel parameters of QISSAT1-2	
Signal output	Analog voltage to off-chip ADC[a]
Pixel pitch	1.1 μm[a]
Pixel thickness	~3 μm[b]
Reset gate	Tapered reset gate[a]
Source follower	Buried channel MOSFET[a]
SF width	0.18 μm[a]
SF length	0.22 μm[a]
Fabrication process	TSMC 45/65 nm 3D BSI CMOS[a]
Pixel substrate	45 nm
ASIC substrate	65 nm
Full-well depth	~210 electrons[c]
Frame rate	Up to 30 fps[d]

[a]Reported in Ref. 14.
[b]Evaluated from fringing within photodetector layer
[c]Reported in Ref. 9.
[d]Reported in Ref. 15.

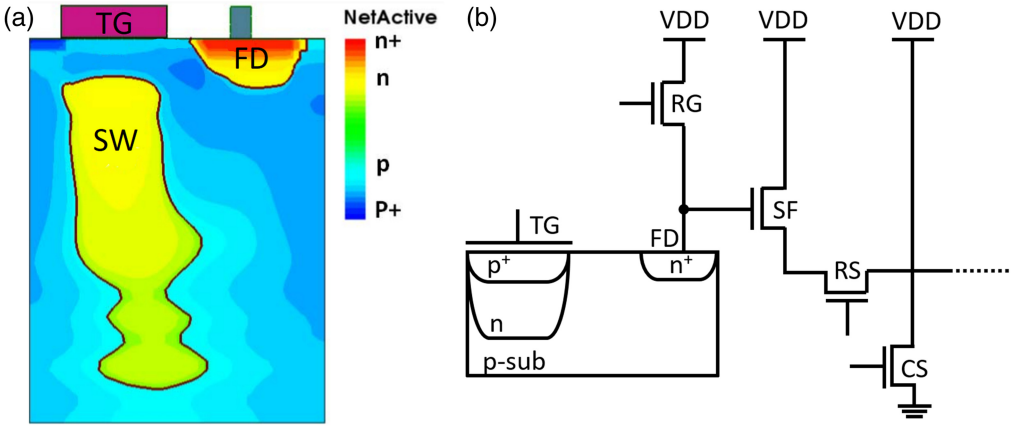

Fig. 2 TCAD-simulated cross-section doping profile of the pixel found in Ref. 17 (a) and a representation of the pixel circuit (b).

To measure incident photons, the FD and storage well (SW) are reverse-biased by shorting the RG and TG. After this, the RG and TG are set to a high-impedance state leaving the pixel floating. As the pixel integrates, incident photons generate signal carriers in the form of electron–hole pairs that migrate toward the SW. Before charge transfer, the FD is sampled multiple times to measure the FD voltage. Real-time correlated multiple sampling hardware averages the samples to calculate the average reset sample. After charge transfer, the system samples the new FD signal and subtracts the average signal sample from the average reset sample to calculate the change in voltage from the transferred charge. The system connects to each FD via the row select and column select.

2 Hardware Test System

The hardware test system consists of a vacuum cryogenic dewar (Fig. 3) and a custom electronics system. A Lakeshore temperature controller monitors and holds the detector temperature with

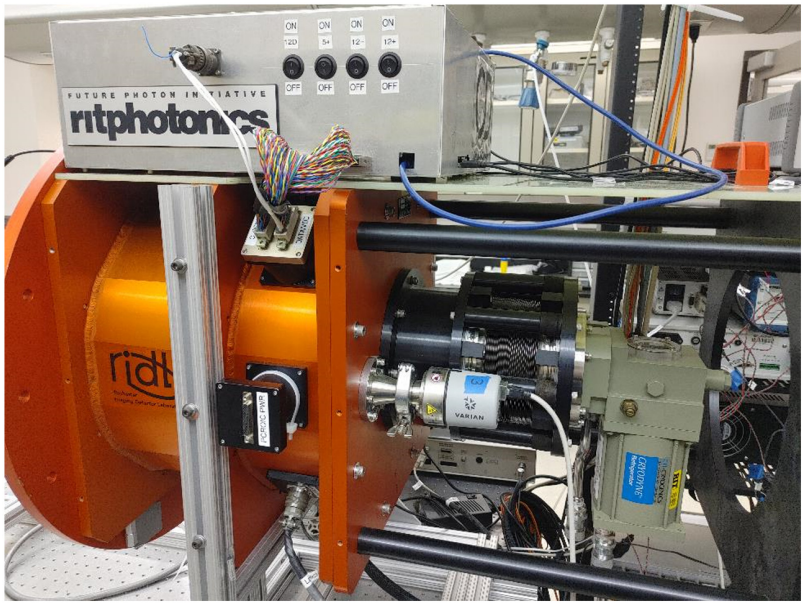

Fig. 3 Dewar with the custom warm electronics mounted on top used for detector testing.

a thermal stability of less than a millikelvin. The dewar has ports where the detectors can be positioned. For radiation testing, we use a side port with a thin aluminum plate to minimize the activation of hardware exposed to the beam.

The system includes electronics located inside the dewar (cold) and outside the dewar (warm). The warm electronics include power supplies and an off-the-shelf field programmable gate array (FPGA) that runs a custom hardware program. The hardware program is responsible for generating detector clocks, programming the cold electronics, receiving data from the analog-to-digital converter (ADC), and sending data to a computer interface. The cold electronics are located inside the dewar. They produce detector clocks, generate bias voltages and currents, measure the analog output voltages from the detector, and convert those voltages into digital numbers. The computer receives raw data from the FPGA, deinterlaces the image, and saves it to memory in real time.

3 Methods

The team characterized a 1-megapixel QIS CIS before and after exposure to high-energy protons. The device was exposed to a 60-MeV proton beam up to a total dose of 50 krad(Si). The following sections describe radiation damage effects in silicon detectors, simulations of radiation on a space mission at L2, and the ground-based radiation test program. The radiation test program used procedures from Refs. 18–20 and is similar to other programs.[21–24]

3.1 Radiation Damage in Silicon Image Sensors

High-energy radiation environments degrade detectors over time due to accumulated damage and single-event effects (SEEs). Radiation damage mechanisms in semiconductor materials fall under three general categories: DDD, total ionizing dose (TID), and SEEs.[25,26] For silicon, the effects of a charged particle passing through the detector may (1) displace atoms from their lattice sites increasing thermal excitation of valence electrons at lattice defects (DDD), (2) generate charge traps at the silicon–oxide interface and material (TID), and (3) induce a local over-density of ionized charges that produce latch ups and SEEs.[25,27] The work in this paper focuses on TID and DDD effects and will not discuss SEE in detail.

3.1.1 *Total ionizing dose effects*

Charged particles and electromagnetic radiation ionize atoms along their trajectory through photosensitive materials, generating electron–hole charge carriers.[28] The energy deposition from

the ionizing radiation leads to the buildup of oxide-trapped charge and the generation of Si/SiO_2 interface traps degrading the electrical characteristics of CMOS devices.[29] Charge trapping near and/or at the semiconductor oxide interface can result in a number of aging mechanisms in advanced CMOS technologies.[30] One aging mechanism is the voltage shift of the pixel output and biases, e.g., threshold and flat-band voltage shift in charge coupled device (CCDs) and CMOS devices.[31–34] As metal-oxide semiconductor (MOS)-based devices (CCDs, CMOS) use a metal–insulator–semiconductor silicon dioxide structures, threshold and flat-band shifts change the sense node output voltage, which may lead to the bias voltage range of sensor circuits limiting instrument lifetime in Mrad dose environments.[35,36]

3.1.2 *Displacement damage dose effects*

High-energy particles can permanently damage a detector by colliding with lattice nodes as they pass through.[37] The displacement damage from the collision generates vacancy–interstitial pairs, most of which immediately recombine.[38] Vacancies that survive will migrate in the lattice and form stable defects. This alters the electrical and optical performance of the device as charge carrier generation and recombination can now pass through new localized energy states in the band gap.

3.2 Simulating Radiation Effects

We simulate the radiation environment and shielding using the Space Environment Information System (SPENVIS).[39] The simulations provide justification for the ground-based test requirements in regard to particle type and mean energy. This section describes simulation results on the radiation abundance and effects on the detector from solar-emitted particles (SEP), trapped ions, and galactic cosmic rays (GCRs). We use the results to justify using 60-MeV protons as can be found at a mono-energetic beamline facility to provide the TID and DDD.

SPENVIS models the unshielded fluence for solar-emitted particles, trapped ions, and GCRs. We use Geant4 tools and choose to model the attenuation through 1 cm of aluminum telescope shielding, as there is no clearly defined telescope structure and instrument shielding for a future NASA mission, such as the Habitable Worlds Observatory. The simulation calculates TID as a function of shielding thickness and DDD by convolving the shielded fluence with silicon's non-ionizing energy loss (NIEL) spline for protons.

Figure 4 shows the integrated fluence of SEP protons, GCR protons, trapped electrons, and trapped protons for an 11-year mission at L2.[39] Integral fluence is the total number of particles

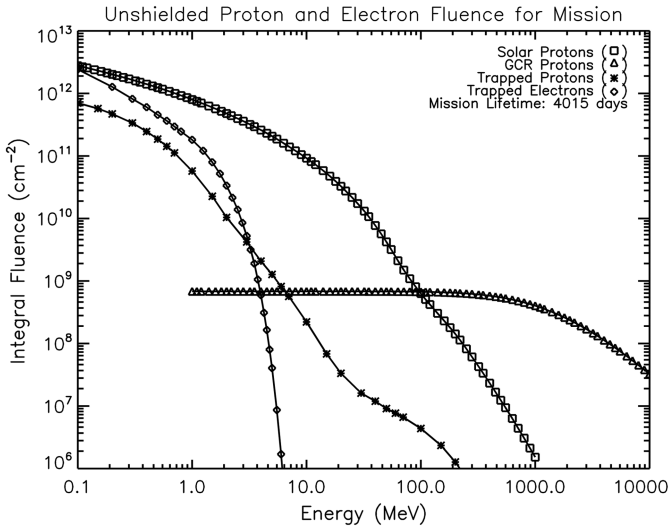

Fig. 4 Plot showing the unshielded radiation environment at L2. Solar protons are taken from the emission of solar protons model. Trapped ions use AP-8 MAX and AE-8 MAX models, and GCR protons use ISO-15390.

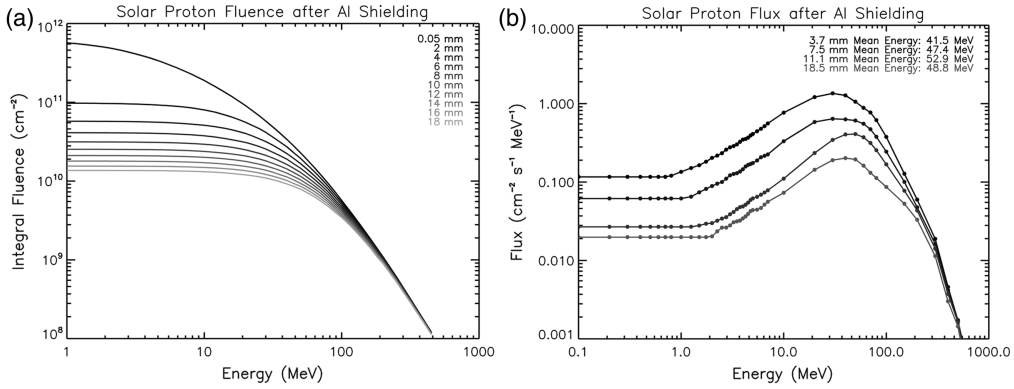

Fig. 5 Attenuated solar proton integral fluence (a) and flux (b) as a function energy for a sensor at L2 with variable thickness Al shields.

with energy at or greater than a given energy. We model solar protons using a near-Earth interplanetary orbit generated from a combination of James Webb Space Telescope and wide-field infrared survey telescope (WFIRST) orbital parameters, including a direct transfer orbit. During the transfer orbit, a spacecraft passes through trapped ions in Earth's magnetosphere. The GCR background fluence is $\sim 7 \times 10^8$ protons/cm^2 throughout the 11-year mission, corresponding to a GCR background rate of ~ 2 protons/cm^2/s. This rate is comparable to the rate experienced by the Gaia, geostationary operational environmental satellite, and ACES telescopes, cumulatively, which measure a continuum particle background of 1 to 3 counts/cm^2/s.[40,41] However, Gaia was launched and operated following the peak activity of solar cycle 24. During this solar cycle, the number of SEP events was much less than expected and the ratio of GCR protons to SEP protons for Gaia's first 72 months is likely much higher than the total mission average for future missions. The simulations presented in this paper integrate over an 11-year solar cycle (4015 days). They show that solar protons with energies in the range of 10 to 100 MeV dominate the abundance of particles over 11 years at L2 while matching the same GCR background as measured by Gaia.

SPENVIS transports the shielded environment through generalized telescope shielding using the Multi-layered Shielding Simulation Software.[42] The model shield is a spherical aluminum shell with a variable thickness. Figure 5 shows the mean proton energy shifts when passing through shielding. For 1 cm of aluminum, the mean proton energy incident on the detector is ~50 MeV where the abundance of solar protons (3×10^{10}) is more than an order of magnitude greater than the >200 MeV GCR background (7×10^8). Of course, a complex telescope structure and its alignment with respect to the sun will attenuate the results presented here and may increase or decrease the ratio of SEP to GCR protons. For example, if multiple detectors are used in a mosaic, some detectors may receive a higher dose than others detectors.[43]

SPENVIS convolves the proton fluence with the NIEL distribution to calculate DDD. We find for 1 cm of shielding, the NIEL weighted spectrum (MeV/g) for protons in the range of 10 to 1000 MeV to peak at a proton energy 52 MeV, with a mean of 59 MeV. For this reason, we choose to expose the detector to 60-MeV protons and because our vacuum hardware requires the protons to pass through a ~2.4-mm-thick aluminum port before it reaches the detector, which decreases the monoenergetic beam energy by ~2 MeV. To compare with studies that use 10-MeV protons such as those used to evaluate the expected radiation damage on detectors in the Gaia telescope,[44] the NIEL curve at 10 MeV is approximately twice the NIEL at 60-MeV protons. A 10-MeV proton beam needs to provide half the number of protons to cause the same DDD as 60-MeV protons.

Figure 6 shows the TID and DDD a detector receives during an 11-year mission at L2. Our ground-based radiation test should provide a TID of ~5 krad(Si) with a DDD of at least 1.18×10^8 MeV/g(Si). For a 60-MeV proton beam, this corresponds to $\sim 3 \times 10^{10}$ protons/cm^2, though we choose to expose the sensor to 3×10^{11} protons/cm^2 or 10 mission equivalent lifetimes.

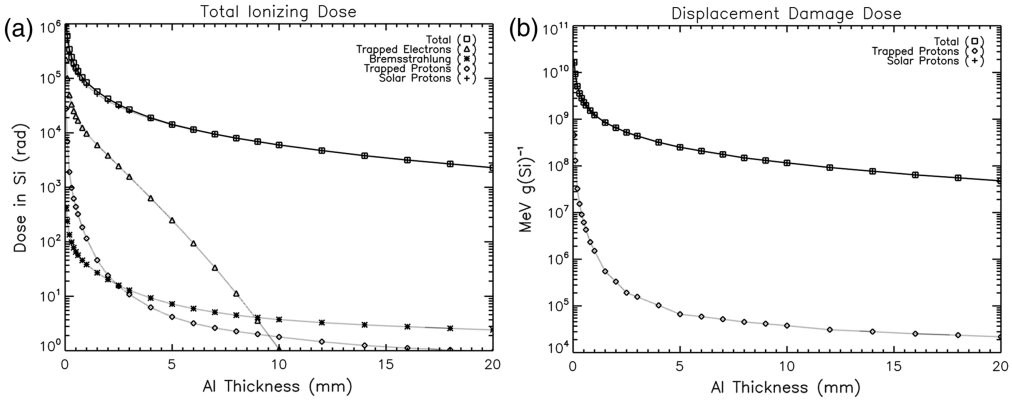

Fig. 6 Total ionizing dose (a) and displacement damage dose (b) as a function of Al shield thickness for one solar cycle.

3.3 Radiation Test Program

The team conducted the radiation test program at the Francis H. Burr Proton Therapy Center at the Massachusetts General Hospital (MGH) (Fig. 7). MGH houses a 230-MeV cyclotron where the proton beam can be directed to one of four gantries. For this experiment, we had the MGH technician calibrate the beam to a mean proton energy of (60.0 ± 2.8) MeV within a 3-in. uniform circle centered on the detector before the beam intensity falls off. We exposed the device to incremental cumulative proton doses of 0.1, 0.2, 0.5, 1, 2, 5, 10, 20, and 50 krad(Si) to evaluate detector performance up to 10 consecutive solar cycles (110 years). We operated the detector at 300 K despite our intention to operate at 200 K due to power supply issues for our compressor and chiller that were only found once on site. At this higher temperature, we expect the detector to anneal at a faster rate than at 200 K.[45] From the results in this paper, we found a space-based QISSAT image sensor would satisfy the Large Ultraviolet Optical Infrared Surveyor (LUVOIR) dark current requirement 0.002 $e^-/s/pix$ at 260 K, much warmer than 200 K.[46]

After assembly, the system captured a series of dark frames every 60 s, one 4.3-ms and one 1060-ms integrations (Sec. 4.2). Before the test, we turned the system off and moved it aside to calibrate the beam alignment and fluence. The facility technician calibrated the beam profile and location using a radiochromic film (Fig. 8) and calibrated fluence and mean energy using an EMC-4 Faraday cup with a 13-mm aperture connected to a Keithley 6517A electrometer.

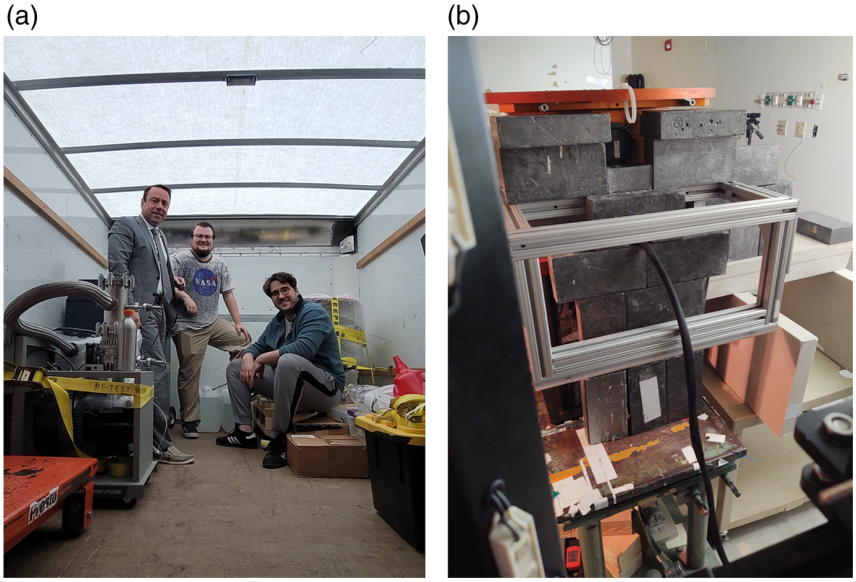

Fig. 7 Two pictures of the radiation test program showing equipment ready for transportation to MGH (a) and the dewar with lead bricks in the beam line (b).

(a) (b)

Fig. 8 Radiochromic film after it was used to verify the alignment and beam profile (a) and the film taped on the dewar port before calibration (b).

The electronics applied power and bias voltages to the detector array before, during, and after each irradiation. Before each exposure to radiation, the sense node and photodiodes were reset and reverse-biased. Then, the reset gate and TG were opened with the TG held at a negative bias (−1.8 V). The electronics did not actively capture frames (read and reset clocks) during irradiation, thus leaving pixels floating during irradiation. At the end of each exposure, the electronics immediately resumed data capture of dark frame pairs. After 20 pairs, the software halts data capture and alerts the team to begin the next dose of radiation.

After the program, the team disassembled the system and transported it back to the lab. Within 24 h, they reassembled the system and verified that the performance did not change between disassembly and reassembly.

4 Results

The pre- and post-radiation performance results include dark current, read noise, conversion gain, QE, and detector bias voltage shift. Post-radiation results for dark current, read noise, conversion gain, and QE were captured after a 36-h anneal with the detector annealing at 314 K. The detector temperature for voltage shift and measurements during irradiation was 302 K. The detector temperature is 200 K unless otherwise reported in the figure legend.

4.1 Dark Current

Dark current is the signal generated in a pixel when devoid of light. It is typically reported in $e^-/s/pixel$ or $pA/s/cm^2$ for CIS. The dominant dark current mechanisms are from (1) the thermal excitation of electrons in the pixel bulk material, (2) the generation of charge at the silicon–oxide interface, and (3) quantum tunneling. Dark current is the slope of a linear fit to an integrated signal as a function of time in a dark environment from a hundred frames per integration time (Fig. 9).

At higher temperatures, the dark current shows a non-linear effect at short (0.1 s) and long (~6 s) integration times. This is due to pixels with an output voltage above or below the voltage range of the analog readout circuit, i.e., "at the rail." As the analog readout circuits use one common mode voltage and the output voltage will vary from pixel to pixel, it is possible the readout circuit connects to a pixel with an output voltage outside the rails. Combining this with an on-chip programmable gain amplifier (PGA), a significant number of pixels (>10%) will be at the voltage rail of the readout circuit. For example, a PGA gain of 10× decreases a 2-V ADC sampling range to 0.2 V. Post-processing software identifies pixels that are at the rail and masks these pixels.

Dark current may also be evaluated from the mean dark current per pixel (Fig. 10). A noticeable tail persists at higher dark currents showing more than 70% of pixels to be lower than the mean dark current after irradiation compared with 55% before. The mean dark current increased from 0.0063 to 0.083 $e^-/s/pixel$. The median dark current increased from 0.0044 to 0.030 $e^-/s/pixel$.

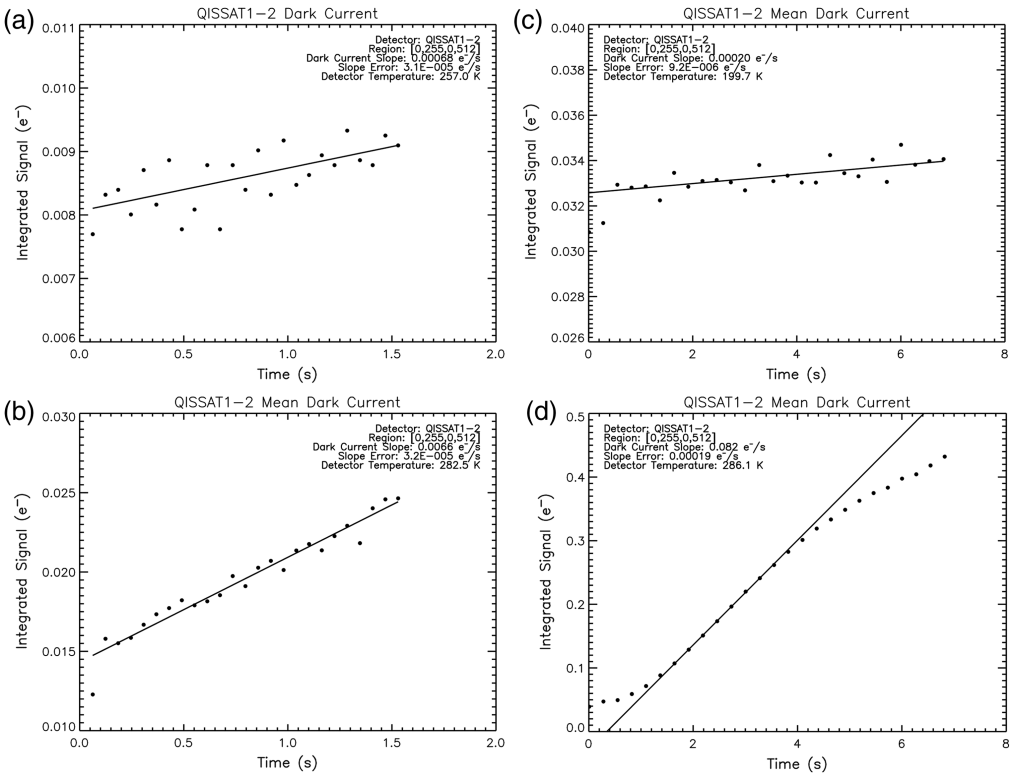

Fig. 9 Sensor dark current: two plots of dark current before radiation (a), (b) and two plots of dark current after radiation (c), (d).

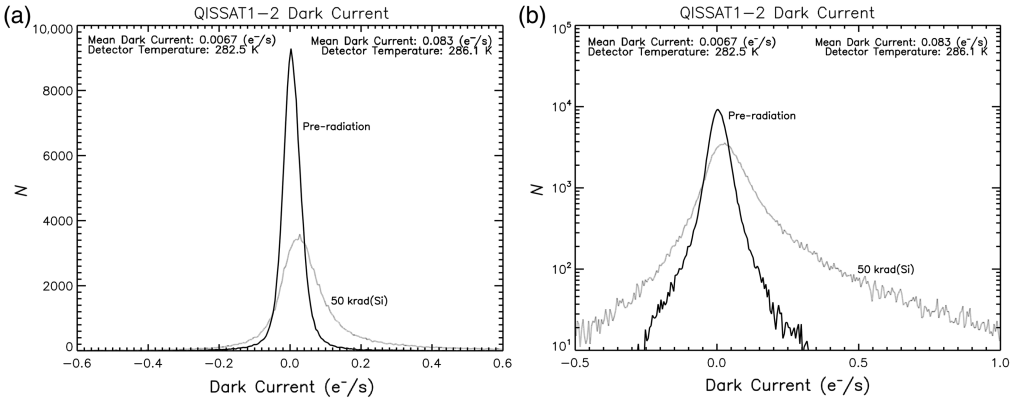

Fig. 10 Dark current distribution before and after radiation in linear (a) and log (b) scale. The width of the distribution increased after radiation with a noticeable tail at higher dark current.

Figure 11 shows the pre- and post-radiation dark current for the QISSAT1-2 over a range of 200 to 300 K. The median dark current increased by an order of magnitude from 0.00085 to 0.0085 $e^-/s/pix$ at 258 K and from 0.0075 to 0.075 $e^-/s/pix$ at 282 K. This implies a mean dark current increase of 2.0 $fA/cm^2/krad(Si)$ at 258 K and 17.8 $fA/cm^2/krad(Si)$ at 282 K. Dark current from quantum tunneling, surface generation, and/or leakage current may explain the dark current plateau at temperatures less than 250-K leakage current and is also reported in Ref. 14.

4.2 Integrated Signal during Radiation Program

As explained in Sec. 3, radiation effects can increase dark current and can be measured as the integrated dark signal rate as a function of radiation dose. The electronics measured the dark signal after each cumulative dose to evaluate the change in the detector's dark current

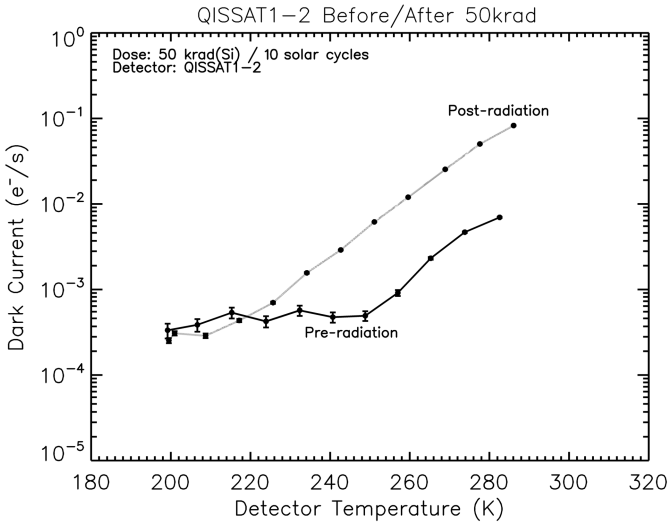

Fig. 11 Plot of QISSAT dark current before (solid) and after (dotted) receiving 50 krad(Si) of 60-MeV protons.

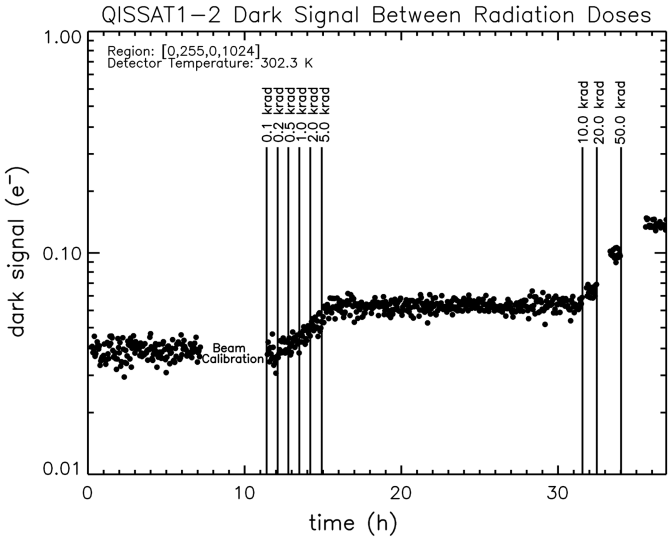

Fig. 12 Plot showing the integrated dark signal between cumulative doses. The signal increases as radiation damage accumulates within the detector.

(Fig. 12). The mean signal before the start of the radiation test program was 0.04 e^-/pixel. This mean signal increased to 0.06 e^-/pixel after 5 krad(Si) and 0.12 e^-/pixel after 50 krad(Si). We did not measure any transient change in signal after each dose including the 16-h capture following the 5-krad exposure.

4.3 Read Noise

Read noise is the measurement uncertainty induced by the readout circuit in the detector. To measure read noise, the device captures dark images with a short integration time (~130 μs). The read noise of a pixel is the standard deviation from multiple dark images (Fig. 13). The read noise varies only slightly, increasing by 2.7% from 0.33 to 0.34 e^- after 50 krad(Si). For CIS, the read noise can increase as gate oxides degrade under increasing doses.[47,48] As the source follower (SF) dominates the QIS read noise, it is likely degradation of the SF oxide will be a dominant factor in the decrease in post-radiation read noise performance. Unexpectedly, there was an increase in pixels on the left side of the distribution with a read noise of 0.20 to 0.23 e^-. The cause of this is not fully understood, but it represents an increase in measurement uncertainty.

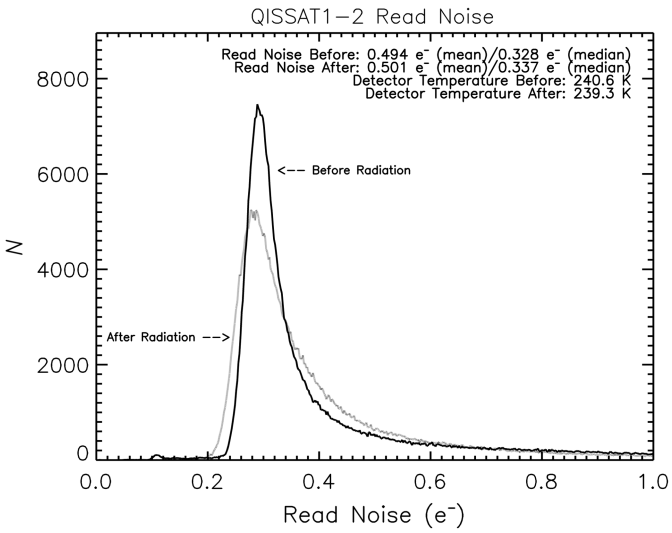

Fig. 13 Plot of the QISSAT read noise before and after radiation.

4.4 Conversion Gain and Single-Photon Counting

Conversion gain is a ratio of the number of analog–digital units of the ADC to the number of electrons integrated in the pixel storage well (ADU/e^-). With photon-number-resolving devices, the conversion gain is the average distance (ADU) between resolved photon peaks.

In the conversion gain experiment, the device captures multiple images under constant uniform illumination. A histogram of pixel measurements shows the so-called photon counting histogram (PCH) (Fig. 14). A custom interactive data language (IDL) PCH fit algorithm determines the location of peaks in the histogram in ADU, over-plots a vertical line for the peak location, and assigns an integer number corresponding to a number of photoelectrons. The conversion gain is the slope of a linear fit to the ADU location as a function of photoelectron number (e^-).

For a given dose of radiation, the number of charge traps in the oxide depends on the thickness of the dielectric layer.[49] The trapped charges cause a shift in threshold voltage and variation of capacitance,[34] resulting in a variation in conversion gain. However, pre- and post-radiation results show the conversion gain (19 ADU/e^-) remained the same as the location of photon peaks did not shift. The photon counting histograms use a region of pixels on the detector array. If the variation of p–n junction capacitance increased due to radiation, the photon peaks would overlap and become indistinguishable. As the center of peaks remained the same, it can be concluded that single-photon sensitivity is not sensitive to doses up to 50 krad(Si). The lack of variation is comparable to other CMOS devices using small node sizes, e.g., a p-type CMOS pixel exposed to more than a Mrad(SiO_2).[50]

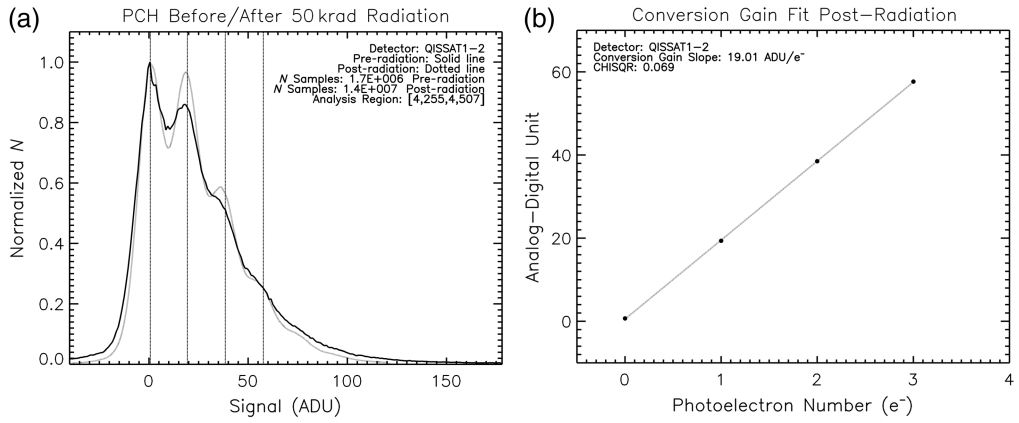

Fig. 14 Photon-counting histogram of multiple pixels before and after radiation (a) and a linear fit to the post-radiation peak locations (b) with a conversion gain slope of 19.01 ADU/e^- for the detector array.

There was a noticeable change in the valley-to-peak separation distance of photon peaks where photon peaks in post-radiation data appear more resolved than pre-radiation data as the post-radiation dataset has an order of magnitude more frames. After 10 solar cycles, the detector still resolves the photon number indicating that both the input referred pixel gain and mean read noise remained in proportion. If the read noise increased, the peaks would maintain their mean value but overlap with neighboring peaks where they are no longer resolved. If radiation damage increased the capacitance of the FD sense node, the input-referred pixel gain would decrease and the mean location of peaks would shift toward zero ADU.

4.5 Quantum Efficiency

QE refers to the efficiency of a detector in registering incident photons into a signal. The team used NIST-traceable calibrated diodes to measure the absolute number of photons, replacing the detector with a diode during system calibration.[51–53] A second diode on the integrating sphere monitors the light level during experiments and system calibration. System calibration records the ratio of measured signal between the calibrated and monitoring diodes over a range of wavelengths (200 to 1200 nm) for both "on" and "off" images, the latter of which occurs when a metal plate blocks the light source at the entrance of the monochromator. The absolute number of photons at the location of the detector is determined via the ratio of the monitoring diode signal during calibration to the signal measured in the QE experiment.

The QE of the QISSAT1-2 had an average change of ~5% to 10% from 500 to 800 nm and did not change significantly beyond 800 nm (Fig. 15). The device has a peak QE of 80% at 480 nm and decreases at longer wavelengths where the device is less sensitive due to the small thickness of the photosensitive layer (~3 μm from Table 1). The QE performance of CIS degrades at shorter wavelengths when exposed to high-energy proton radiation due to displacement damage effects that produce traps in the material.[54] The number of events, or radiation-induced traps, within a pixel will depend on the overall pixel area and volume. As the QISSAT1-2 has pixels that are smaller than other scientific CIS devices, the number of events will be lower with respect to the smaller pixels. However, it is not clear if this will proportionally degrade the QE as this will depend upon the trap location with respect to the pixel circuit elements and bulk flow of charge carriers.

4.6 Inter-pixel Capacitance

Inter-pixel capacitance (IPC) is an effect where charge one pixel influences the performance of neighboring pixels through mutual capacitance among electronic structures associated with a pixel and its neighbors. Although this effect is completely deterministic and can be deconvolved, its impact on low flux signal-to-noise and <1.1 μm pixel pitch devices is being explored.

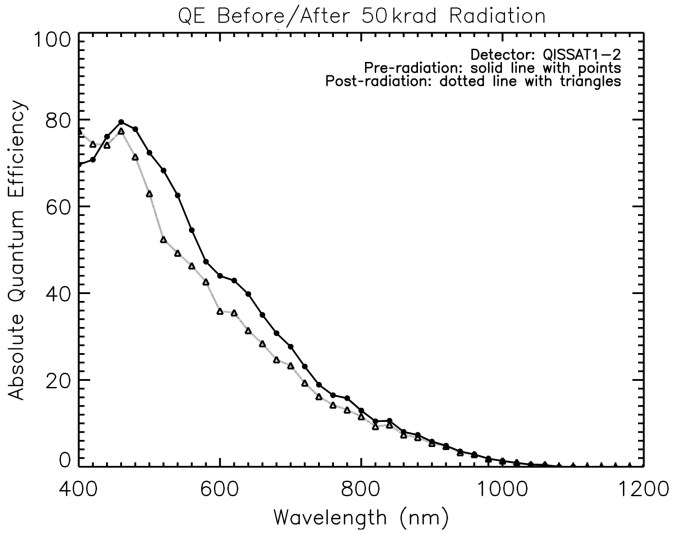

Fig. 15 Plot of QE before and after radiation testing.

(a)

QISSAT1-2 Preradiation IPC (%) Number of Frames: 8750 Number of Events: 481		
−0.09	0.13	−0.03
−0.02	100.00	0.28
−0.03	0.36	0.18

(b)

QISSAT1-2 Postradiation IPC (%) Number of Frames: 8060 Number of Events: 443		
−0.09	−0.16	−0.01
0.36	100.00	0.44
−0.04	−0.68	0.01

Fig. 16 IPC of the QISSAT1-2 device (a) before and (b) after radiation.

The IPC analysis identifies pixels that have a high signal (100σ from the mean of a frame) and symmetric distribution of the signal surrounding them. This type of pattern is taken as a sign that the central pixel was hit with a centrally and normally incident particle, such as a secondary from a cosmic ray shower or high-energy photons from radioactive materials in the environment. After this rejection, the software averages the remaining pixel with neighbors and normalizes the averaged thumbnail to the maximum signal. The normalized QISSAT1-2 IPC results before and after radiation testing are shown in Fig. 16.

For most neighboring pixels, the QISSAT IPC is less than half a percent with a small shift further from an ideal IPC of zero after high-energy radiation. Given that shifts occur in both positive and negative IPC, it is possible the QISSAT IPC was not significantly affected.

Although we consider IPC, we note that the results would also measure the diffusion of charge carriers in the semiconductor bulk from the central pixel to the neighboring pixels but not isolate this effect from IPC. This is known as charge diffusion crosstalk (CDC). As modern CIS pixels continue to shrink to sub-micron sizes, CDC becomes a critical issue to sensor QE performance.[55] CIS devices use deep trench isolation (DTI) structures, physical potential barriers in between pixels, to prevent charge carriers from diffusing among neighboring pixels.[8,28]

As the QISSAT1-2 is based on a pathfinder design for early QIS development, it is possible DTI structures were not yet implemented in the QISSAT1-2, for example, using shallow trench isolation structures instead. If the QISSAT1-2 does not use DTI and CDC is found in Fig. 16, then the overall crosstalk performance will improve with the use of DTI.

4.7 Voltage Shift of the Pixel Output

Figure 17 shows the mean reset voltage of the FDs in the image sensor as a function of proton dose. A voltage shift of 1.2 mV/krad(Si) is measured in the reset samples of the pixel. For 50 krad(Si), the small voltage shift of the QISSAT1-2 is comparable to modern CMOS devices. During space mission, the voltage shift can be mitigated through appropriate adjustment to the operating biases in flight. However, future missions to Europa that encounter greater than 1 Mrad of radiation are expected to see shifts greater than a volt. This shift must be considered for missions that use modern CMOS devices where biases for the sensor have a small range (e.g., 0 to 3.3 V and 0 to 5 V). For example, the QISSAT1-2 has an analog output voltage swing of one volt for a given set electronics gain.

5 Discussion

The following section summarizes the radiation tolerance of the QISSAT, compares the increase in dark current to other detector technologies, and discusses the potential the detector technology has to serve as the baseline detector platform for future NASA missions.

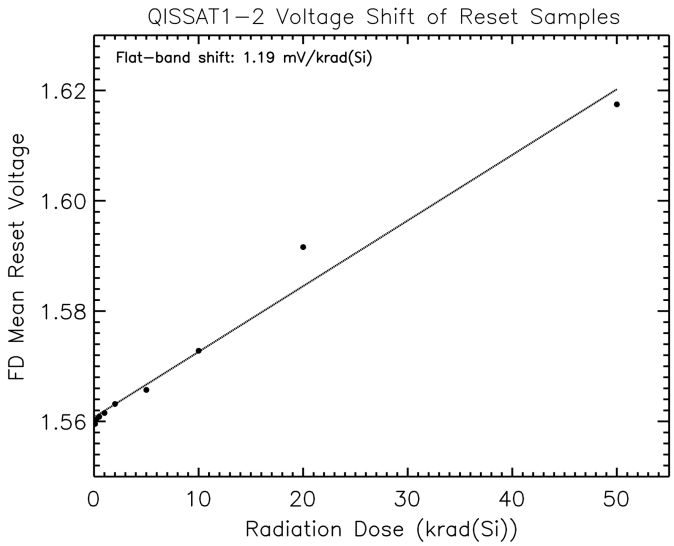

Fig. 17 Plot of mean floating diffusion voltage during reset samples as a function of dose showing a shift of ~1.2 mV/krad(Si).

5.1 Device Testing Summary

After exposure to a 50 krad(Si) dose of 60-MeV protons, the median dark current increased by a rate of 2.0 $\mathrm{fA/cm^2/krad(Si)}$ at 258 K and 17.8 $\mathrm{fA/cm^2/krad(Si)}$ at 282 K. Performance in other metrics, such as 0.34 $\mathrm{e^-}$ median read noise, 85% peak QE at 490 nm, and conversion gain, remained the same.

The increase in dark current is minimal, as the beginning of life performance is maintained by cooling the device an additional 8 K per solar cycle at L2. As the QISSAT1-2 achieves the dark current specification of 0.002 $\mathrm{e^-/pix/s}$ for the High-Definition Imager (HDI) of the LUVOIR concept mission at 262 K, a projected operating temperature of 254 K would maintain the specification well above the baselined temperature of 170 K.[46] This relaxes the thermal design, which may now be satisfied using a simple two-stage thermoelectric cooler.

5.2 Comparison to Other Detector Technologies

The dark current increase as a function of radiation dose for the QISSAT1-2 is compared with other CMOS and CCD devices in Table 2. The results shown here do not categorize the dark current increase to either TID or DDD effects but rather consider the overall increase as the dark current performance is one of the key metrics to consider for future NASA science goals to measure the concentration of gases in the atmosphere of exoplanets.

The authors note it is difficult to find publications with radiation tolerance results for silicon CMOS/CCD image sensors within the last 5 years (Table 2). We include results for a p-type BSI trench-pinned CMOS device, which uses a 90-nm process[50] and is representative of CMOS radiation tolerance when using small (<100 nm) lithography process nodes. The QISSAT1-2 exhibits a comparable radiation tolerance to the expected tolerance of modern CMOS devices.

The detectors in Table 2 were selected as they were exposed to a similar radiation program reported in this work: high-energy protons were used with an energy range of 20 to 100 MeV with a dose of a few to hundreds of krad(Si). For a majority of values in the table, the dark current increase was reported $\mathrm{pA/cm^2/krad}$ or $\mathrm{pA/cm^2}$ and did not need any unit conversion. In more than half of the reported results, the detector temperature was not 20°C but within ±20°C. In these cases, the dark current increase was extrapolated to 20°C using a dark current doubling temperature provided by the respective publication. If doubling temperature was not reported, we used the doubling temperature from Fig. 11. For cases where the dark current was reported in electrons/pixel/second, we converted the pixel to a cross-sectional area via the pixel pitch and converted it into Amps.

Table 2 Dark current increase from radiation damage for various silicon image sensors.

High-energy proton-induced dark current rate at ~20°C		
Device	Thickness (μm)	pA/cm^2/krad
QISSAT1-2 (this work, 50 krad(Si))[a,b]	3	0.043
p-type BSI trench-pinned CMOS (up to 30 krad(SiO_2))[50]	3.5	0.033
p-type BSI trench-pinned CMOS (up to 100 krad(SiO_2))[50]	3.5	0.06
STAR-250 APS[56a]	3	0.30
STAR-250 APS[57a]	3	1.5
Radiation hardened CMOS APS[58]	Not reported	2
e2V FI Jade (BW 204)[59]	6	10
e2V CIS106 (variant 7)[60]	11	18
e2V CIS106 (variant 8)[60]	11	19
e2V FI Jade (BW 206)[59]	6	20
e2V CIS106 (variant 6)[60]	11	21
CCD47-20 (FSI)[31]	25	20
CCD55[56]	25	31
CCD57[56]	25	38
CCD47-20 (BSI)[31]	25	40
e2V FI Jade[59]	6	58
CCD47-20[61a]	25	66
Tektronix 1024CCD[62a]	25	145
CCD[63]	Not reported	2000

[a]Interpolated using doubling temperature from Fig. 11.
[b]Interpolated using data extracted from Fig. 11.

5.3 A DSERN CMOS Detector Platform for NASA Instruments

The radiation tolerance of the QISSAT1-2 is comparable to the tolerance expected from modern commercial-of-the-shelf CIS. The QISSAT1-2 is an early-generation QIS architecture, made to evaluate the performance of design variations to the pixel. This early-generation QIS sensor maintained a dark current lower than the specification for the HDI instrument of LUVOIR. It exceeds the frame rate and noise specifications by more than an order of magnitude, though improvements to the detector NUV/NIR QE and full well depth will bring the device closer to all the detector specifications for future missions (see Sec. 5.4). The detector platform also has potential for missions that aim to study Jupiter's moons. These missions need detectors that operate after exposure to a TID greater than a Mrad due to trapped particles in Jupiter's magnetosphere.[64]

Another key advantage of CMOS devices over CCDs is that they are direct readout devices. They do not suffer from the loss of charges trapped by permanent radiation damage while transferring charge across the detector array. In addition, future instrument designers will need to manage bias voltage shift. For comparison, the PEM-CCD devices on the Gaia Space Telescope were baselined to tolerate a maximum expected bias voltage shift of 0.5 V over 10 years.[65] Over 10 years at L2, Gaia's instruments receive 5 krad of radiation or a voltage shift of 100 mV/krad. Extrapolating this for the Jovian moons, a Gaia-like instrument would need to account for a shift of 100 V. The QISSAT has a bias voltage shift of 1.2 mV/krad or 1.2 V for a Mrad, which is

mostly attributed to the thin oxide thickness. CCDs have a much thicker oxide layer compared with DSERN CMOS. Most oxides in commercial CCDs are thick (~100 nm),[56,66] whereas CMOS devices fabricated with a 45-nm process can achieve oxides less than 1 nm.[67,68]

In addition to great radiation tolerance, DSERN CMOS devices enable future missions to baseline smaller and lighter science instruments. Commercial DSERN CMOS devices use a wide range of pixel sizes spanning from 1.1 up to 4.6 μm. A gigapixel format DSERN CMOS detector array with 2.2-μm pixels would be 65 mm on a side and could perform Nyquist-sampling at 500 nm with an $f/8$ beam, as demonstrated in Ref. 69. Compare this to the larger 6.5-μm pixels baselined for the HDI instrument of the LUVOIR concept mission.[46]

5.4 Suggested Design Improvements

Although the first-generation DSERN CMOS devices have phenomenal performance that already meets or exceeds detector performance requirements for future NASA missions, they were not designed for astrophysical applications. The technology should be scaled to larger pixel pitches with thicker versions for better long wavelength response and versions with backside processing for the best short wavelength response.[70–72] Of course, a thicker device will increase the dark current contribution from the bulk generation–recombination process, though the dark current floor of the QISSAT1-2 is likely not from bulk effects that would decrease with temperature.

Although devices can be mosaicked for gigapixel focal planes, it may be more effective to develop gigapixel detectors. The large format sensor is already segmented and operates with multiple sub-arrays in parallel, thus mitigating against serious faults that might otherwise cause a whole detector to fail. The detector platforms are made using a standard 3D integrated CMOS process employed by the semiconductor industry, leveraging decades of improvements in fabrication to produce high-yield and reliable devices.

One promising area for future development is the use of cosmic ray rejection operational modes that leverage non-destructive reads. Current implementations of DSERN CMOS devices measure the total integrated signal from an exposure by sampling the FD voltage before and after the transfer of the signal. This readout mode is not a limitation of the on-chip circuits but rather the modifiable hardware program that clocks the device that is optimized for commercial applications.

As is often the case for IR detectors, such as the WFC3-IR and NIRSpec detectors,[73] an exposure consists of multiple non-destructive reads throughout the integration. This "up-the-ramp" sampling technique (Fig. 18) is useful because the effect of a cosmic ray hit is identifiable and can be removed from the data during post-processing. When a cosmic ray hits a pixel, a significant jump in the rate is observed, which detection software uses to split the ramp into

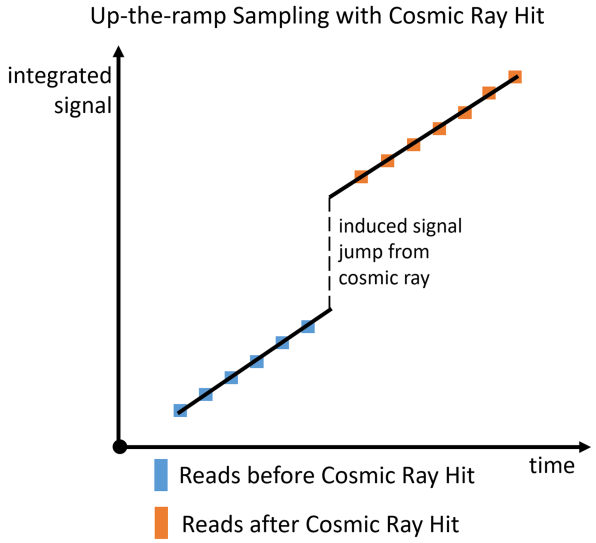

Fig. 18 Up-the-ramp sampling technique and the induced signal jump of a cosmic ray hit. The jump can be identified and removed.

separate segments. The software fits and averages the slopes in the segments to best estimate the signal rate, removing the cosmic ray effect, and preserving the exposure.[74–76]

6 Conclusion

The image sensor presented in this paper offers the possibility of large-format single-photon counting and photon-number resolving CIS for use in future NASA missions recommended by the decadal survey. It delivers several important advantages for astronomy projects. Many of these benefits overlap very well with future needs, including needs not satisfied by any existing technologies, and are as follows:

1. The DSERN allows single-photon counting.
2. The photon counting leads to low noise re-binning and coadding measurements.
3. The pixels are demonstrated in a range of sizes from 1.1 to 4.6 μm, increasing the design flexibility for future science instruments.
4. The potential for very small pixels leads to small detectors and thus small instruments. For example, a critically sampled diffraction-limited point spread function would require an $\sim f/8$ beam.
5. Small pixels provide for instrument designs that could have oversampled focal planes without increasing noise or reducing the field of view. This feature would be advantageous in applications that require precise measurement of centroids (e.g., lucky imaging) and/or measurement of object shapes (e.g., weak lensing).

The high performance of the technology at room temperature yields new design phase space for science instruments and attendant technologies (i.e., readout and refrigeration), allowing dramatic reductions in size, weight, and power for focal planes up to gigapixel formats.

Disclosures

The authors have no relevant financial interests in the paper and no other potential conflicts of interest.

Code and Data Availability

Data reported in this paper will be free for reuse. The Flexible image transport system though data contain significant intellectual property and will only be shared in response to requests that do not jeopardize confidentiality.

Acknowledgments

The results presented in this paper are supported by the NASA Strategic Astrophysics Technology (SAT) Program (Grant No. 80NSSC20K0310).

References

1. C. E. A. Stark, "ExoEarth yield landscape for future direct imaging space telescopes," *J. Astron. Telesc. Instrum. Syst.* **5**(2), 024009 (2019).
2. J. Wang et al., "Baseline requirements for detecting biosignatures with the HabEx and LUVOIR mission concepts," *J. Astron. Telesc. Instrum. Syst.* **4**(3), 035001 (2018).
3. National Academies of Sciences, Engineering, and Medicine, *Pathways to Discovery in Astronomy and Astrophysics for the 2020s*, The National Academies Press, Washington, DC (2021).
4. J. Ma, S. Chan, and E. R. Fossum, "Review of quanta image sensors for ultralow-light imaging," *IEEE Trans. Electron Devices* **69**(6), 2824–2839 (2022).
5. E. R. Fossum, "What to do with sub-diffraction-limit (SDL) pixels?—a proposal for a gigapixel digital film sensor (DFS)," in *IEEE Workshop on Charge-Coupled Devices and Adv. Image Sens.* (2005).
6. E. R. Fossum, "The quanta image sensor (QIS): concepts and challenges," in *Imaging and Appl. Opt. Tech. Digest* (2011).
7. E. Fossum and D. Hondongwa, "A review of the pinned photodiode for CCD and CMOS image sensors," *IEEE J. Electron Devices Soc.* **2**(3), 33–43 (2014).

8. J. Ma and E. R. Fossum, "A pump-gate jot device with high conversion," *Electron Devices Soc.* **3**(2), 73–77 (2015).
9. J. P. Gallagher et al., "Characterization of single-photon sensing and photon-number resolving CMOS image sensors," *Proc. SPIE* **12191**, 121910T (2022).
10. J. Ma et al., "A 0.19e- rms read noise 16.7 Mpixel stacked quanta image sensor with 1.1 μm-pitch backside illuminated pixels," *IEEE Electron Device Lett.* **42**(6), 891–894 (2021).
11. J. Ma et al., "A photon-counting 4Mpixel stacked BSI quanta image sensor with 0.3 e-read noise and 100 dB single-exposure dynamic range," in *Symp. on VLSI Circuits* (2021).
12. J. Ma et al., "A 1.26-inch 40.7 mega-pixel photon-counting quanta image sensor with 0.35e- read noise and 95 dB single-exposure dynamic range," in *Imaging and Appl. Opt. Congr.*, Vancouver (2022).
13. J. Ma et al., "Ultra-high-resolution quanta image sensor with reliable photon-number-resolving and high dynamic range capabilities," *Sci. Rep.* **12**, 13869 (2022).
14. W. Deng, "Noise performance of quanta image sensors," Thesis, Thayer School of Engineering Dartmouth College (2022).
15. J. Ma et al., "Photon-number-resolving megapixel image sensor at room temperature without avalanche gain," *Optica* **4**(12), 1474–1481 (2017).
16. J. Ma, L. Anzagira, and E. R. Fossum, "A 1 μm-pitch quanta image sensor jot device with shared readout," *IEEE J. Electron Devices Soc.* **4**(2), 83–89 (2016).
17. J. Ma and E. Fossum, "Quanta image sensor jot with sub 0.3e- r.m.s. read noise and photon counting capability," *IEE Electron Device Lett.* **36**(9), 926–928 (2015).
18. E. Daly et al., "Standards for space radiation environments and effects," in *Proc. 7th Eur. Conf. Radiation and Its Effects on Components and Systems*, IEEE, pp. 175–179 (2003).
19. L. D. Edmonds, C. E. Barnes, and L. Z. Scheick, *An Introduction to Space Radiation Effects on Microelectronics*, JPL Publication, Pasadena (2000).
20. D. Everett and L. E. A. Hartz, "General environmental verification standard (GEVS) GSFC-STD-7000B," 28 April 2021, https://standards.nasa.gov/sites/default/files/standards/GSFC/B/0/gsfc-std-7000b_signature_cycle_04_28_2021_fixed_links.pdf.
21. K. Kolb et al., "Test results for an array-based GM-APD detector before and after irradiation," in *Proc. Sci. Detect. Workshop* (2013).
22. K. Kolb et al., "Radiation tolerance of a Geiger-mode avalanche photodiode imaging array," *J. Astron. Telesc. Instrum. Syst.* **2**(3), 036001 (2016).
23. Z. Lee-Payne and J. Skottfelt, "Long term effects of irradiation on CCDs under mission representative conditions," *Proc. SPIE* **12191**, 121910D (2022).
24. H. Becker et al., *Commercial Sensor Survey Fiscal Year 2008 Compendium Radiation Test Report*, Jet Propulsion Laboratory, Pasadena, California (2008).
25. J. Srour, R. Hartmann, and K. Kitazaki, "Permanent damage produced by single proton interactions in silicon devices," *IEEE Trans. Nucl. Sci.* **33**(6), 1597–1604 (1986).
26. J. Srour, C. Marhsall, and P. Marhsall, "Review of displacement damage effects in silicon devices," *IEEE Trans. Nucl. Sci.* **50**(3), 653–670 (2003).
27. E. Fossum et al., "CMOS active pixel image sensor containing pinned photodiodes," *NASA Tech. Briefs* **20**(10), 40–42 (1996).
28. J. Tan, B. Büttgen, and A. Theuwissen, "Radiation effects on CMOS image sensors due to X-rays," in *The Eighth Int. Conf. Adv. Semicond. Devices and Microsyst* (2010).
29. V. Goiffon et al., "Radiation effects in pinned photodiode CMOS image sensors: pixel performance degradation due to total ionizing dose," *IEEE Trans. Nucl. Sci.* **59**(6), 2878–2887 (2012).
30. V. Huard, "Two independent components modeling for negative bias temperature instability," in *IEEE Int. Reliab. Phys. Symp.*, Anaheim, CA, USA (2010).
31. D. Burt et al., "Improving radiation tolerance in e2v CCD sensors," *Proc. SPIE* **7439**, 743902 (2009).
32. C. Marhsall and P. Marshall, *CCD Radiation Effects and Test Issues for Satellite Designers*, NASA Electronic Parts and Packaging (NEPP) Program's Electronics Radiation Characterization (ERC) Project and the Defense Threat Reduction Agency's (DTRA) Radiation Hardened Microelectronics (RHM) Program (2004).
33. T. Oldham, *Basic Mechanisms of TID and DDD Response in MOS and Bipolar Microelectronics*, DSFG, Inc, NASA Goddard, Radiation Effects and Analysis Group (2012).
34. J. Schwank et al., "Radiation effects in MOS oxides," *IEEE Trans. Nucl. Sci.* **55**, 1833–1853 (2008).
35. J. Tan, B. Buttgen, and A. Theuwissen, "Analyzing the radiation degradation of 4-transistor deep submicron technology CMOS image sensors," *IEEE Sens. J.* **12**(6), 2278–2286 (2012).
36. J. Prinzie, M. Steyaert, and P. Leroux, *Radiation Effects in CMOS Technology*, pp. 1–20, Springer (2018).
37. G. Hopkinson and A. Mohommadzadeh, "Radiation effects in charge-coupled devices (CCD) imagers and CMOS active pixel sensors," *Int. J. High Speed Electron. Syst.* **14**(2), 419–443 (2004).

38. A. Bardoux et al., "Radiation effects on image sensors," *Proc. SPIE* **10564**, 105640M (2012).
39. M. Kruglanski et al., "Space Environment Information System (SPENVIS)," in *38th COSPAR Sci. Assembly*, July, Vol. 38, p. 8 (2010).
40. C. Kirsch, *The Cosmic Ray Background at L2 as Seen in Gaia Observations*, Friedrich-Alexander-Universität Erlangen-Nürnberg, Erlangen, Germany (2018).
41. S. Ahmed et al., "Understanding the evolution of radiation damage on the Gaia CCDs after 72 months at L2," *J. Astron. Telesc. Instrum. Syst.* **8**(1), 016003 (2022).
42. F. Lei et al., "MULASSIS: a Geant4-based multilayered shielding simulation tool," *IEEE Trans. Nucl. Sci.* **49**(6), 2788–2793 (2002).
43. G. Seabroke, A. Holland, and M. Cropper, "Modelling radiation damage to ESA's Gaia satellite CCDs," *Proc. SPIE* **7021**, 70211P (2008).
44. D. Smith and A. Holland, "Proton irradiation of e2v technologies L3Vision devices," *Nucl. Instrum. Methods Phys. Res. Sect. A: Accel. Spectrom. Detect. Assoc. Equip.* **546**(3), 544–552 (2005).
45. H. Hughes and J. Benedetto, "Radiation effects and hardening of MOS technology: devices and circuits," *IEEE Trans. Nucl. Sci.* **50**(3), 500–521 (2003).
46. The LUVOIR Team, "The LUVOIR mission concept study interim report," 2019, https://asd.gsfc.nasa.gov/luvoir/reports/LUVOIR_FinalReport_2019-08-26.pdf (accessed 2020).
47. S. Place et al., "Radiation effects on CMOS image sensors with sub-2 μm pinned photodiodes," in *12th Eur. Conf. Radiat. and Its Effects on Components and Syst.*, pp. 314–320 (2011).
48. D. Fleetwood et al., "Unified model of hole trapping, 1/f noise, and thermally stimulated current in MOS devices," *IEEE Trans. Nucl. Sci.* **49**(6), 2674–2683 (2002).
49. A. Karmakar et al., "A review of semiconductor based ionising radiation sensors used in harsh radiation environments and their applications," *Radiation* **1**, 194–217 (2021).
50. A. Atonsanti et al., "Ionizing radiation effects on hole collection backside-illuminated p-type deep-trench-pinned photo-MOS pixels under image acquisition," *IEEE Trans. Nucl. Sci.* **70**(8), 1958–1965 (2023).
51. P. Hammarstedt, "Development of a system for absolute quantum efficiency determination of hybrid photo diodes," CERN Document Server, Geneva (2001).
52. B. Jacquot et al., "A system and methodologies for absolute QE measurements from the vacuum unltraviolet through the NIR," *Rev. Sci. Instrum.* **82**(4), 043102 (2011).
53. A. Migdall et al., *Single-Photon Generation and Detection: Physics and Applications*, Experimental Methods in the Physical Sciences ed. 45, Academic Press (2013).
54. L. Ma et al., "Analysis of proton and γ-ray radiation effects on CMOS active pixel sensors," *Chin. Phys. B* **26**(11), 114212 (2017).
55. Y. Yamashita et al., "Quantum efficiency simulation and electrical cross-talk index development with Monte-Carlo simulation based on Boltzmann transport equation," *ITE Trans. Media Technol. Appl.* **6**(3), 180–186 (2018).
56. G. Hopkinson, R. Harboe-Sorensen, and A. Mohammadzadeh, "Radiation testing of CCD and APS," in *QCA Presentation Day*, 11 May (2004).
57. J. Bogaerts et al., "Total dose and displacement damage effects in a radiation-hardened CMOS APS," *IEEE Trans. Electron Devices* **50**(1), 84–90 (2003).
58. E.-S. Eid et al., "Design and characterization of ionizing radiation-tolerant CMOS APS image sensors up to 30 Mrd (Si) total dose," *IEEE Trans. Nucl. Sci.* **48**(6), 1796–1806 (2001).
59. B. Dryer, "Characterisation of CMOS APS technologies for space applications," PhD thesis, Open University (2013).
60. A. Pike, J. Pratlong, and T. Greig, "Comparison of proton damage effects in standard and enhanced depletion CMOS image sensors," in *14th Eur. Conf. Radiat. and its Effects on Components and Syst. (RADECS)* (2013).
61. N. Bassler, "Radiation damage in charge-coupled devices," *Radiat. Environ. Biophys.* **49**(3), 373–378 (2010).
62. A. Delamere et al., "Radiation test results on TK 1024 CCDs," (1990).
63. A. Holmes-Siedle and L. Adams, *Handbook of Radiation Effects*, 2nd ed., Oxford University Press (2002).
64. T. Bayer et al., "Europa Clipper mission: the habitability of an icy moon," in *IEEE Aerosp. Conf.*, Big Sky, MT, USA (2015).
65. C. Crowley et al., "Gaia Data Release 1: on-orbit performance of the Gaia CCDs at L2," *Astron. Astrophys.* **595**(A6) (2016).
66. M. Robbins et al., "Quality control and monitoring of radiation damage in charge coupled devices at the Stanford Linear Collider," *IEEE Trans. Nucl. Sci.* **40**(6), 1561–1566 (1993).
67. A. Duba et al., "High K oxides as an alternative gate oxide in CMOS technology and its corresponding effects," *Int. J. Eng. Res. Technol.* **2**(11), 732–739 (2013).

68. N. Sachdeva and M. Vashishath, "Design, simulation & optimization of 45 nm NMOS transistor," *Int. J. Adv. Res. Comput. Commun. Eng.* **5**(1), 272–274 (2016).
69. L. Buntic, D. F. Figer, and J. P. Gallagher, "Evaluating detector requirements for the next UV/O/IR flagship observatory," *Proc. SPIE* **12191**, 121911L (2022).
70. M. Hoenk et al., "Delta-doped back-illuminated CMOS imaging arrays: progress and prospects," *Proc. SPIE* **7419**, 74190T (2009).
71. R. Westhoff et al., "Radiation-hard, charge-coupled devices for the extreme ultraviolet variability experiment," *Proc. SPIE* **6686**, 668604 (2007).
72. P. O'Connor et al., "Study of silicon sensor thickness optimization for LSST," *Proc. SPIE* **6276**, 62761W (2006).
73. M. Robberto, *Analysis of the Sampling Schemes for WFC3-IR*, STScI (2007).
74. J. Offenberg et al., "Cosmic ray rejection with NGST," in *Astron. Data Anal. Softw. and Syst. VIII*, Vol. 172, p. 141 (1999).
75. D. Fixsen and J. Offenberg, "Up-the-ramp processing and cosmic ray rejection with limited memory," in *Proc., IEEE Aerosp. Conf.*, Big Sky, MT, USA (2002).
76. G. Giardino et al., "The impact of cosmic rays on the sensitivity of JWST/NIRSpec," *Publ. Astron. Soc. Pac.* **131**(1003), 094503 (2019).

Justin P. Gallagher is the chief laboratory engineer at the Center for Detectors within the Rochester Institute of Technology. He serves as the project engineer for multiple National Aeronautics and Space Administration (NASA)- and National Science Foundation-funded programs to develop optical and near-infrared single-photon-counting large format detector arrays. He received his BS degree in physics and his MS degree in astrophysical sciences and technology from Rochester Institute of Technology in 2020. He designs, develops, and deploys photon devices to enable scientific discoveries.

Lazar Buntic is a graduate student at the Rochester Institute of Technology, pursuing a doctorate in instrumentation for astrophysics. He received his BS degree in astronomy and astrophysics from the Pennsylvania State University in 2018. His research interests focus on detector development for astrophysics research, primarily for optical and infrared wavelengths. He is particularly interested in the impact of improved detector performance on mission design for future NASA observatories.

Wei Deng is a pixel development engineer at Apple Inc. He received his PhD in engineering sciences from the Thayer School of Engineering at Dartmouth College in 2022 and his BS degree in physics from Nankai University, Tianjin, China, in 2016. His research interests include low-noise and high-speed quanta image sensors and CMOS image sensors and their applications.

Eric R. Fossum is the John H. Krehbiel Sr. Professor for Emerging Technologies with the Thayer School of Engineering, Dartmouth College. He is the primary inventor of the CMOS image sensor. He was awarded the IEEE Andrew Grove Award, the Queen Elizabeth Prize for Engineering in 2017, the OSA/IS&T Land Medal in 2020, the Technical Emmy Award in 2021, and the IS&T Electronic Imaging Scientist of the Year in 2022.

Donald F. Figer is a professor and director of the Center for Detectors and the Future Photon Initiative at Rochester Institute of Technology. He developed detectors for the Hubble Space Telescope and the James Webb Space Telescope (JWST). He received numerous awards, e.g., the NASA Space Act Award for characterizing competing JWST prototype detectors and the AURA STScI Technology and Innovation Award for founding the Independent Detector Testing Laboratory at Johns Hopkins University.